

The effect of target properties on crater morphology: Comparison of central peak craters on the Moon and Ganymede

Veronica J. BRAY^{1,3*}, Gareth S. COLLINS¹, Joanna V. MORGAN¹, and Paul M. SCHENK²

¹Earth Science and Engineering Department, Imperial College London, Exhibition Road, London SW7 2BP, UK

²Lunar and Planetary Institute, 3600 Bay Area Blvd., Houston, Texas 77058, USA

³Lunar and Planetary Laboratory, University of Arizona, Tucson, Arizona 85721, USA

*Corresponding author. E-mail: vjbray@lpl.arizona.edu

(Received 23 March 2008; revision accepted 01 December 2008)

Abstract—We examine the morphology of central peak craters on the Moon and Ganymede in order to investigate differences in the near-surface properties of these bodies. We have extracted topographic profiles across craters on Ganymede using Galileo images, and use these data to compile scaling trends. Comparisons between lunar and Ganymede craters show that crater depth, wall slope and amount of central uplift are all affected by material properties. We observe no major differences between similar-sized craters in the dark and bright terrain of Ganymede, suggesting that dark terrain does not contain enough silicate material to significantly increase the strength of the surface ice. Below crater diameters of ~12 km, central peak craters on Ganymede and simple craters on the Moon have similar rim heights, indicating comparable amounts of rim collapse. This suggests that the formation of central peaks at smaller crater diameters on Ganymede than the Moon is dominated by enhanced central floor uplift rather than rim collapse. Crater wall slope trends are similar on the Moon and Ganymede, indicating that there is a similar trend in material weakening with increasing crater size, and possibly that the mechanism of weakening during impact is analogous in icy and rocky targets. We have run a suite of numerical models to simulate the formation of central peak craters on Ganymede and the Moon. Our modeling shows that the same styles of strength model can be applied to ice and rock, and that the strength model parameters do not differ significantly between materials.

INTRODUCTION

Impact cratering is a complex process that depends upon the size, velocity and composition of the impacting body, as well as the gravity and near-surface properties of the target. As a result of the latter, the study of impact craters offers a tool for investigating the subsurface structure and composition of solar system bodies. For example, the crater diameter at which small bowl-shaped “simple” craters develop into “complex” craters (those with terraced or slumped crater rims, flat floors and additional central features such as central peaks or peak-rings; see Melosh 1989) is approximately inversely proportional to the target body’s gravity (Pike 1977, 1988), but is also affected by differences in target properties (Head 1976; Grieve 1987).

The surfaces of the Galilean satellites of Ganymede and Europa are composed primarily of water ice (Showman et al. 2004), making craters on these bodies useful for studying impact into ice. Craters on these bodies exhibit the same simple and central peak morphologies seen for craters below

~150 km in diameter on the Moon. However, the largest craters on the icy Galilean satellites display exotic morphologies that have no obvious lunar analogues (e.g., large central pits; see Fig. 5d) (Croft et al. 1985; McKinnon et al. 1991). As the gravities of Ganymede and Europa are similar to the Earth’s moon (1.43 m s^{-2} and 1.33 m s^{-2} , respectively, relative to 1.63 m s^{-2} for the Moon), the unusual crater morphologies are considered to be due to the mechanical properties of ice or the presence of subsurface liquid layers (e.g., Moore et al. 2001; Schenk 2002).

An important goal of future research is to determine whether impact crater morphology can be used to estimate ice thickness as it has implications for the accessibility and habitability of these putative subsurface oceans (e.g., Chyba 2000). This requires further understanding of the crater formation process in ice before the crater morphologies created as a result of subsurface layering can be differentiated from those occurring as a direct result of the cratering process in ice. As the ice crust of Ganymede is thicker than that of Europa, the morphologies of its smaller craters are expected

to be relatively unaffected by the presence of its subsurface ocean (Schenk 2002), and thus provide a suitable source for observations of craters that have formed in unlayered ice.

The use of computer modeling has advanced investigation of the impact process, allowing complex crater collapse to be studied on planetary scales. Before a numerical modeling approach can be used to estimate ice layer thickness, we must first better determine the mechanical properties of ice, as hydrocodes rely on accurate strength models to recreate the material behavior during crater formation.

This paper is split into two parts. First, we present existing observational data for the Moon and Ganymede, and new topographic profiles of central peak craters on Ganymede, created from Galileo photogrammetry and stereo photogrammetry. These profiles are used to create scaling trends which are then compared to existing lunar and Ganymede trends. The differences in lunar and Ganymede crater scaling are discussed and used to infer differences in the near-surface properties of these two bodies. In the second part of the paper, we present results of simulated crater formation in rock and ice using dynamic modeling codes, testing results by comparison with observational data, similar to previous works (e.g., Turtle and Pierazzo 2001; Collins et al. 2002). We compare our icy impact model results with the observed topographic profiles and scaling trends of Ganymede craters, and use these comparisons to determine the range of target strength parameters that can produce a reasonable match between the modeled and observed data. These values are then compared to model parameters for lunar craters, and used to draw additional information on the differences between the surfaces of the Moon and Ganymede.

OBSERVATIONS

Method

Topographic mapping of planetary surfaces is commonly based on a combination of direct shadow measurement, photogrammetry, stereo image analysis and where possible laser altimetry, and has been completed for the Moon and Galilean satellites (e.g., Smith et al. 1997; Schenk et al. 2001). The lack of laser altimetry of the Galilean satellites restricts height measurements of surface features to image-based methods. For information on stereo and photogrammetric techniques see Efford (1991) and Jankowski and Squyres (1991).

The majority of current topographic data available for Ganymede is based on Voyager images that have a maximum horizontal resolution of ~ 0.5 km per pixel. This resolution translates to uncertainties on depth measurements of between 10 and 30% (Schenk 1991). Higher resolution Galileo data has been used to refine depth-diameter plots and measurements (e.g., Schenk 2002), with systematic errors on

depth measurements of $\sim 5\%$ (Schenk et al. 2004); crater wall slopes and other measurements requiring height data have not yet been presented. Height measurements based on these higher-resolution data are expected to be of higher accuracy, especially with regard to small diameter craters. However, the lower number of craters imaged by Galileo will lead to a higher apparent variability of the crater dimensions.

We used a combination of Galileo stereo and photogrammetry to produce topographic profiles of 38 craters on Ganymede, including 19 fresh central peak craters which range in size from 4.7 km to 50.4 km in diameter, and host peak widths of 1.7 to 25 km. The freshest craters on Ganymede display highly variable bright and dark deposits on their floors and rims (Schenk and McKinnon 1991). As the accuracy of digital elevation models (DEMs) derived via photogrammetry is highly affected by surface albedo variations, we restricted our measurements to slightly more mature central peak craters that have lost most of their extreme albedo deposits while remaining morphologically crisp.

The Ganymede surface is separated into distinct bright and dark terrains which are believed to consist of pure ice, and an ice-rock mix, respectively (Breneman and Belton 1998). The dark terrain is considered to be older than the bright terrain, and to have undergone larger degrees of mass-wasting processes on account of its higher (albedo-induced) temperature (Moore et al. 1996). Terrain type was noted at the time of profile collection so that any differences in crater trends on bright and dark terrains could be documented.

Our photogrammetry incorporated the combined lunar-Lambert photometric function as defined by McEwen (1991), and was chosen over other options such as the Minnaert function on account of its greater applicability, especially near the limb and at moderate to high phase angles. Our stereo data was created from Galileo Solid State Imager (SSI) data, with the use of the scene-recognition algorithm developed by Schenk et al. (2004). Once each DEM of a crater was obtained, spurious patterns or shape distortions created by radiation noise or data compression artefacts were removed through the use of standard image noise filters, and manually by visual inspection of the DEM and original image(s). Data gaps, deep shadows and features superimposed after impact were also removed.

We acquired 6 to 8 radial profiles across each crater, pairing when possible to create 3 to 4 full cross sectional profiles; crater diameters (D) were determined from an average of the 3 to 4 rim-to-rim distances. Measurements of other crater dimensions and internal features were made from all radial profiles of each crater (Fig. 1); this gave a range of values for each crater characteristic, which have been used to determine error bars. Errors stated in this work are inclusive of both morphologic variation and errors inherent to the photogrammetry/stereo process. Obvious outliers in these values were discarded and the maximum reasonable value

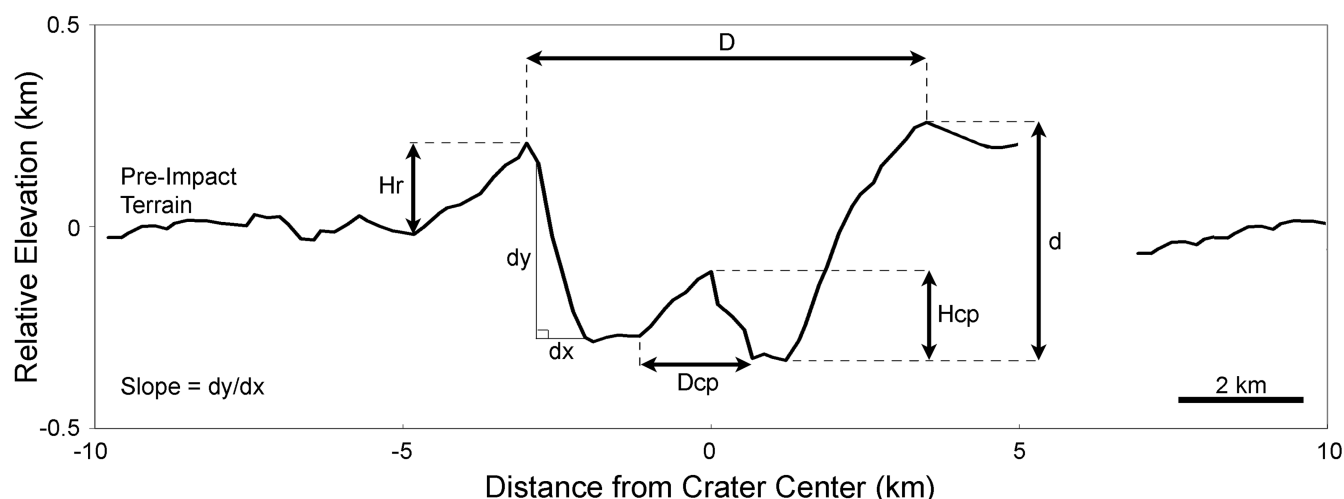


Fig. 1. Annotated topographic cross section of a 7 km diameter crater on dark terrain at 22.6° N, 194.1° W. Vertical exaggeration is 9.5×. D is the rim-to-rim diameter; d is the crater depth, measured from the maximum rim elevation to the lowest point on the crater floor. The height of the crater rim above the average surrounding terrain level (the rim height) and maximum elevation of the central peak summit above the crater floor (the central peak height) are noted with H_r and H_{cp} , respectively. D_{cp} is the diameter of the central peak. In cases of a two-tiered central peak (see Fig. 5b), the peak diameter was measured as the base of the top “tier” and did not include the lower “tier” breadth. The average wall slope calculation is noted.

adopted for each feature measurement prior to the construction of scaling trends; height and width values in this work should therefore be viewed as an upper bound.

In cases where the topographic data was created via stereo and the local terrain was not significantly disrupted by later impact or fracturing, the profile was extended up to 5 crater radii so that the pre-impact terrain surface could also be recorded (Fig. 1); this enabled the pre-impact terrain slope to be removed from the profiles, allowing easy comparison with computer simulation results, for which the pre-impact surface is represented by a smooth horizontal plain. In cases of extreme topographic tilt, craters with morphologic features deemed to be anomalous were not included in the data set.

Existing and New Data

Depth-Diameter Ratios

Observational data for lunar craters has revealed a linear relationship between depth (d) and diameter (D) of impact craters of the type $d = \alpha D$ where α is a constant of proportionality approximately equal to 0.2 for simple craters (Pike 1977). Simple craters are deeper relative to the crater diameter, than larger complex craters, resulting in a shallower d/D trend line (Pike 1977; Schenk 2002). On the Moon this change in d/D ratio occurs at ~11 km (Pike 1977).

The depth-diameter relationship of fresh Ganymede craters has shown simple craters on Ganymede to have a similar d/D slope to that of lunar craters (Schenk 1991). The depth of complex craters on Ganymede increases with increasing crater diameter, similar to lunar craters (Fig. 2). However, complex craters on Ganymede are inherently 60–70% shallower than lunar craters of the same diameter

(Croft 1981). The s-c transition diameter for craters on Ganymede was first estimated at 3 to 5 km by Passey and Shoemaker (1982) and later refined by Schenk (1991) on the basis of Voyager data to 5 ± 1 km. This value was updated after more accurate Galileo measurement to reveal a smaller s-c transition diameter of 1.9 ± 0.5 km (Schenk 2002).

In addition to the change in d/D ratio associated with the s-c transition at crater diameters of ~2 km, Schenk (2002) recorded a further two transitions in d/D ratio at larger crater sizes. The first occurs at ~26 km is associated with a subtle decrease in crater depths and the transition from central peak morphology to central pit craters (Fig. 5d). Another, sharper reduction in crater depth occurs after ~60 km and marks the development of anomalous crater morphologies. Both changes in d/D ratio are thought due to temperature-induced transitions in rheology at depth (Schenk 2002).

The depth and diameter of the fresh craters profiled in the course of this work are presented in Fig. 2. As simple craters were not included in this work, the s-c transition is not discussed. There is a possible break in the d/D trend line at $D \sim 20$ km that corresponds with the appearance of flat-floored craters (see Melosh 1989). Tentative power-law trend line gradients of 0.47 and 0.36 could be assigned to crater depths of craters between 5 to 20 km and 20 to 50 km, respectively. However, as more depth measurements of craters in the 20 to 50 km diameter range are needed to confirm this, we have fitted a general trend line for craters up to 50 km in diameter of $d = 0.23 D^{0.45}$ which includes central peak and flat-floored craters. Above $D \sim 50$ km, central pit morphology becomes prevalent and crater depths reduce further, producing a roll over in the d/D trend line to a power law gradient of -0.41.

Table 1. Summary of scaling trends for the Moon and Ganymede.

Properties	Moon		Ganymede–Voyager		Ganymede–Galileo	
	Dependence on crater diameter, D	D range (km)	Dependence on crater diameter, D	D range (km)	Dependence on crater diameter, D	D range (km)
Crater depth, d	$0.196 D^{1.01\ddagger}$ $1.044 D^{0.301\ddagger}$	<11 11–400	$0.088 D^{0.989*}$ $0.22 D^{0.44*}$	0.4–1.4 >5	$D^{0.2***}$ $0.227 D^{0.446}$	<1.9 (± 0.5) 5–50
Rim height, H_r	$0.036 D^{1.014\ddagger}$ $0.236 D^{0.399\ddagger}$	<21 21–400	$H_r = D^{1.061*}$	<14.2	$0.045 D^{0.772}$ $0.085 D^{0.365}$	<12 12–35
Peak diameter, D_{cp}	$0.22 D^{\dagger\dagger}$	20–140	$D_{cp} = 0.3 D^{**}$	<14	$0.300 D$	5–50
Peak height, H_{cp}	$0.006 D^{1.28\ddagger\ddagger}$ $0.0006 D^{1.969\ddagger\ddagger}$ $\sim 3\ddagger$	>35 17–51 80–200	$0.0004 D^{2.557*}$ $0.09 D^{0.429*}$	<15 >15	$0.0018 D^{1.54}$	12–50

Sources: \dagger Pike 1977; $\dagger\dagger$ Pike 1985; $\ddagger\ddagger$ Wood 1973; \ddagger Hale and Grieve 1982; *Schenk 1991; **Passey and Shoemaker 1982; ***Schenk 2002.

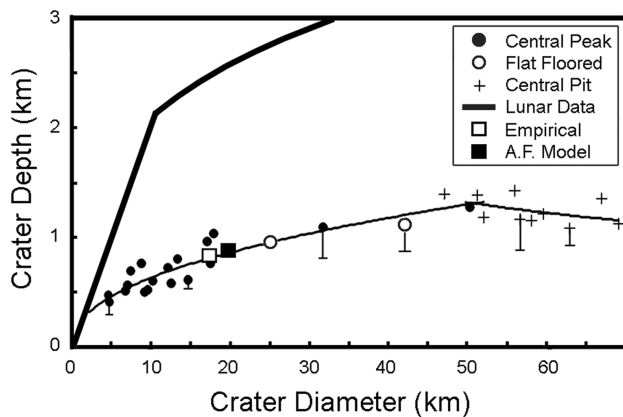


Fig. 2. Depth-diameter plot of craters on Ganymede. Different crater morphologies are noted and a lunar trend included for comparison (Pike 1977). The thin black line shows the least-squares fit to data from this work; error bars are representative. Best-fit results from our numerical modeling using an empirical strength model and one applying acoustic fluidization (A. F.) are marked with square data points (see section Numerical Modeling of Crater Formation in Ice).

Rim Heights

The height of crater rims is thought to offer indirect evidence of the extent of crater wall collapse (Melosh 1989; Schenk 1991). Rim heights (H_r) of craters on the Moon have been documented by Pike (1976) and found to be proportional to crater diameter (D). A break in the H_r/D ratio occurs at a diameter of ~ 21 km (Table 1) and indicates significantly more collapse occurring in craters larger than this diameter. Rim heights on Ganymede were measured by Schenk (1991) using a combination of Voyager photoclinoetry and shadow measurements, and were found to increase with crater diameter, following a log-log slope of ~ 0.98 up to diameters of 10 to 15 km (Table 1; Fig. 3). More obvious wall slump was observed for craters above this diameter; larger craters have a smaller H_r/D ratio due to the relatively shorter rim heights and wider rim-to-rim crater diameters produced by the additional collapse. Schenk (1991) found the break in H_r/D slope to occur at $D = 14.2$ ($+9.6$, -5.7) km.

The rim height measurements for craters below ~ 12 km in diameter from Voyager photoclinoetry (Schenk 1991) are

consistently 20% shorter than our new measurements from Galileo-based photoclinoetry (Fig. 3). This is likely due to Voyager's lower image resolution and has resulted in differing trend lines for the smaller craters (Table 1); Voyager and Galileo-based rim height trends are consistent for the larger craters. The height of the crater rim above the pre-impact terrain level increases as crater size increases, as seen in lunar craters (Fig. 3a); however, the relative rim height (H_r/D) decreases (Fig. 3b). Below 11.85 ($+2.25$, -1.5) km diameter, the Ganymede and lunar trends are similar. After this diameter the increase in rim height with increasing crater size is significantly less, and the lunar and Ganymede trend lines diverge. Ganymede crater rims become at least 50% lower than lunar craters of the same size. Both relations are included in Table 1.

Crater Wall Slopes

The target strength values inferred from analysis of the s-c transition are significantly below the static strength values expected for rock and ice on the basis of laboratory strength tests, suggesting that the target material has an "effective" strength during impact formation that is lower than its "static" value (Melosh 1977; McKinnon 1978). The walls of complex craters include scarps, terraces and scree slopes segments, analysis of which can provide information on the material strength and target structure (e.g., Nycz and Hildebrand 2007). The average wall slope angle is also a useful diagnostic tool when considering the large-scale movement of the target material during impact crater formation. As slope angle is a proxy for the "effective" coefficient of friction (μ_{eff}), measurement of average crater wall slope angles (S) allows μ_{eff} of the target material during the process of impact crater formation to be estimated; this approach is not applicable when determining the "static" coefficient of friction of the target material prior to or after impact.

The average wall slopes of lunar craters above 15 km in diameter decrease as crater diameter increases from 29° to 14° for 10–60 km craters (Pike 1976). This decrease in slope angle demonstrates an effective weakening of the target material during impact as crater size increases from $\mu_{\text{eff}} = 0.55$ to 0.25. A kink in the slope of S/D plots is also observed (Pike 1977), corresponding with the s-c transition. This is

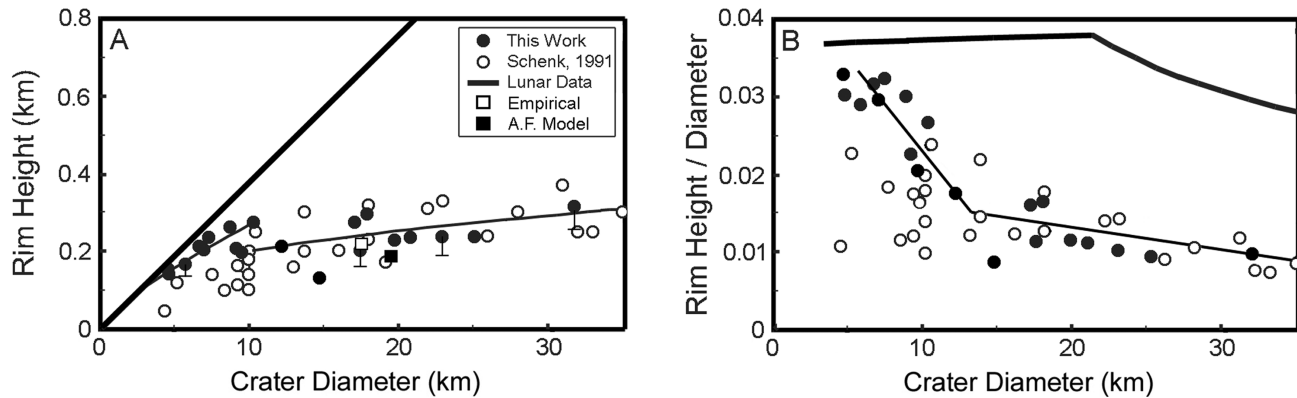


Fig. 3. a) Rim height and crater diameter measurements of craters on Ganymede. b) Relative rim height trend. Measurements from Galileo (this work) and Voyager data (Schenk 1991) are shown with closed and open circles, respectively. The narrow line shows the least squares fit to the data. For craters below ~ 12 km, this trend line is based on Galileo data alone; above this crater diameter, the trend line is based on the combined Voyager and Galileo data sets. Representative number of error bars included. The heavy line is the corresponding trend for lunar craters (Pike 1977). Best-fit results from our numerical modeling are marked with square data points.

attributed to the additional amount of collapse from the rim of complex craters increasing diameter while decreasing the rim height (Pike 1980).

A decrease in wall slope with crater size has also been observed for Ganymede (Wood 1973), where a variation of wall slope between 15° and 35° has been noted (Schenk 1991). A break in the S/D curve is recorded at a similar diameter to the change in the H_r/D ratio and correlates with the identification of slump features in Ganymede craters above 15 ± 5 km (Schenk 1991); terraces on Ganymede crater walls are less pronounced than in lunar craters (Schenk 1991 2002).

We recorded average wall slopes ranging from 5° to 25° for craters in both bright and dark terrain. These average crater wall slopes are consistently shallower than for similar-sized craters on the Moon by up to 50% (Fig. 4). The wall slopes of Ganymede craters above 10 km in diameter decrease as crater diameter increases from 24° for a 10 km crater, to 17° for 50–60 km craters, a similar decrease to that observed in lunar craters.

Central Peak Morphology

Central peaks are thought to form via uplift of the transient crater floor during the modification phase of impact crater formation (see Melosh 1989). It is intuitive therefore that the larger the impact, the greater the amount of central uplift. This is reflected by the positive correlation of central peak diameter (D_{cp}) and height (H_{cp}) with crater diameter noted on both the Moon and Ganymede (Passey and Shoemaker 1982; Pike 1985; Schenk 1991). Central peaks on Ganymede are recorded as being $\sim 25\%$ wider than central peaks in the same diameter lunar craters (Moore et al. 1985; Schenk 1989).

Our measurements support previous observations that central peak diameters on Ganymede are typically 1/3 of the crater diameter (Table 1). We report a positive trend in peak

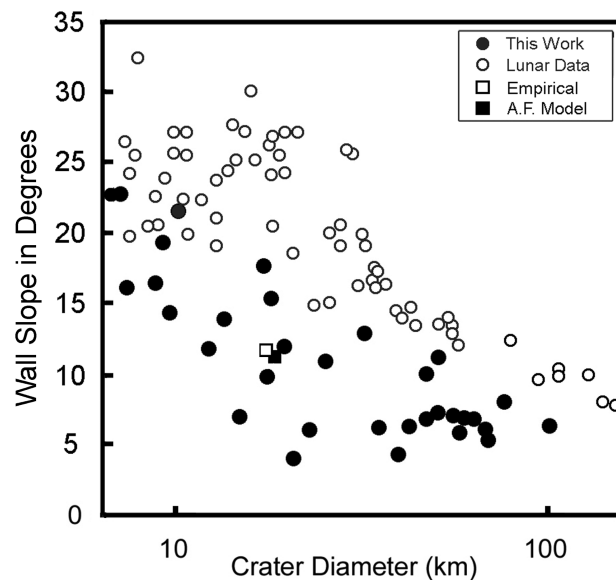


Fig. 4. Wall slope and diameter measurements of craters on Ganymede (this work). Lunar data is from Pike (1976). Lunar and Ganymede wall slopes are shown with closed and open circles, respectively. Errors in slope measurement are $\sim 5\%$ and incorporated in the data point size. Best-fit simulation results are marked with square data points.

height for craters above 12 km in diameter, although crater peak heights below this crater size do not follow published data. Instead, we report a highly variable central peak height, ranging from 50 to 550 m, with an average of ~ 200 m (Table 1).

A series of central peak crater profiles is presented in Fig. 5, showing the general morphological trend as crater size increases. In craters below 30 km in diameter central peaks are mainly conical in shape (e.g., Fig. 5a), although some off-center and asymmetrical examples were recorded. Central peaks generally remain below the level of the pre-impact

surface and certainly below the crater rim level. The larger central peak craters that were profiled in this work show peak heights in excess of the pre-impact surface and the crater rim (e.g., Fig. 5b). These large central peaks are also observed to have a two-tiered morphology with a notably wider base. This morphology is also seen of the European summit-pit crater Cilix, and several central pit craters on Ganymede. In the largest central peak crater profiled in this work this wide peak base is replaced by a concentric topographically expressed uplift between the central peak and the crater rim (Fig. 5c). Such concentric internal features are also observed to surround the summits of central pit craters (Fig. 5d) and increase in diameter with increasing crater size (Bray 2008).

Observational Summary and Implications

Our selection of crater profiles provides a representative sample of fresh central peak crater morphology on Ganymede. The higher resolution of Galileo SSI data has allowed the trends for smaller craters to be updated relative to Voyager measurements. This section summarizes our findings and discusses the implications of differences in the lunar and Ganymede scaling trends.

Degree of Crater Collapse

For crater diameters below 11.85 (+2.25, -1.5) km, the rim height trends of simple craters on the Moon and complex craters on Ganymede are similar, suggesting a common controlling factor in the rim collapse, despite the contrasting crater types (Fig. 3). As Ganymede has a slightly lower gravity than that of the Moon, rim heights might be expected to be subtly larger on Ganymede. However, rims on Ganymede decrease in height relative to their lunar counterparts as crater size increases, demonstrating progressively more rim collapse in ice. This disparity is more extreme for craters above ~12 km where the lower relative rim heights of craters on Ganymede indicate significantly more rim collapse, which is presumably due to the ice-rich target.

The separate rim height trend for craters above and below ~12 km suggests that a strength threshold is exceeded at this diameter which prompts more rigorous collapse in larger craters. This is separate from the s-c transition at 1.9 ± 0.5 km (Schenk 2002), showing that central floor uplift and rim collapse in complex craters are not necessarily connected processes. This suggests that the earlier s-c transition on Ganymede relative to the Moon may be the result of more rapid floor uplift due to weaker material at depth, rather than weaker surface ice allowing the onset of rim collapse at smaller crater diameters. As central peak formation does not appear to require significant rim collapse, numerical models must be able to produce central peak morphology by another means.

Effective Strength of the Target During Crater Formation

Crater wall slopes on Ganymede are shallower than those in lunar craters of the same size (Fig. 4). This shows the surface ice to have a lower effective coefficient of friction than lunar rock during impact crater formation. There is no obvious difference between the wall slopes of craters in dark and bright terrain showing that the additional rock content of the dark terrain does not provide significant strengthening to the surface ice.

Average wall slopes of Ganymede craters decrease as crater size increase, demonstrating an effective weakening of the target as impact event size increases. This decrease in wall slope is similar on the Moon and Ganymede (Fig. 4) indicating the same trend in material weakening with crater size on these two satellites. This suggests that the mechanism of material weakening during impact is similar in icy and rocky targets, and that existing lunar-style material strength models may also be appropriate for impact simulations on icy bodies.

Central Peak Development

The progression in central peak morphology, from a conical shape (Fig. 5a) to a two-tiered slope with a wide base (Fig. 5b), suggests that the central peak has become gravitationally unstable and started to collapse downwards and outwards. As peak collapse progresses further the basal sections may develop into the concentric ring morphology seen in Fig. 5c. These rings are likely to be connected with internal crater development rather than rim collapse as they occur inside the maximum distance from the crater rim expected for mega-terraces (Pearce and Melosh 1986). The features could thus be produced as the result of outward moving peak material colliding with collapsing rim debris, similar to a suggested mechanism for peak-ring formation (Morgan et al. 2000; Collins et al. 2002; Osinski and Spray 2005). Alternatively, such concentric topographic uplifts could be explained by multiple vertical oscillations of the crater's central region; this would provide support for the Bingham plastic model for peak-ring formation (Melosh 1982; Alexopoulos and McKinnon 1994).

NUMERICAL MODELING OF CRATER FORMATION IN ICE

Approach to Modeling

We simulate impact crater formation on the Moon and Ganymede using the iSALE hydrocode, a multi-rheology, multi-material extension of the SALE hydrocode (Amsden et al. 1980), specifically developed to model impact crater formation in its entirety (Melosh 1992; Ivanov et al. 1997; Collins et al. 2004). Hydrocodes rely on accurate constitutive models and equations of state (EoS) to correctly describe the material

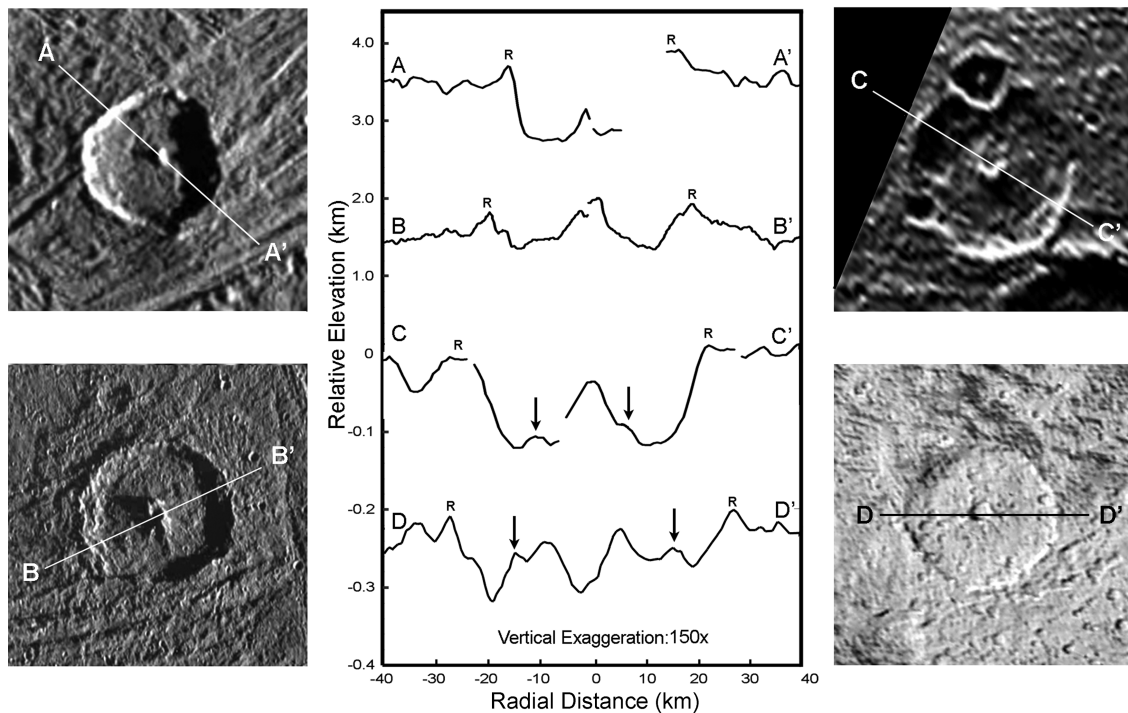


Fig. 5. Topographic profiles across a selection of Ganymede craters. A shows a central peak crater, B shows a central peak crater with a small pit at the center of its central peak, C shows a larger central peak crater, and D shows a central pit crater. Profiles A and B are from photoclinoimetry; C and D are from stereo photogrammy. Crater rims are labelled with "R", proposed internal ring structures are marked with arrows. Artefacts and regions of high shadow have been removed. North is up in all images.

behavior during impact, and to recreate the appropriate amount of crater collapse. In the later stages of cratering, when the cratering flow is essentially incompressible and the deep excavated cavity collapses under gravity, the constitutive (or strength) model is of primary importance. It is this phase of crater formation that is believed to have the most profound effect on crater shape, leading to the diverse range of observed complex crater morphologies.

The basis for any impact strength model is the static strength of the material; this can be derived from laboratory strength tests of the material at high pressure. In addition to a material's standard response to applied stress as measured in a laboratory, it is generally accepted that a further weakening mechanism must be included in the constitutive model for impact events (e.g., Melosh 1989). Material weakening during impact may be achieved to some extent by the intensive fracturing of the target and by thermal softening, both of which are included in the iSALE hydrocode (Ohnaka 1995; Ivanov et al. 1997). However, the formation of central peaks and peak-rings indicates a fluid-like movement during complex crater collapse, necessitating a different style of weakening. The nature of this fluidization is poorly understood at present and several weakening mechanisms have been suggested. These are outlined by Melosh (1989) and include thermal softening (O'Keefe and Ahrens 1993, 1999), interstitial fluid and melt fluidization (Spray and Thompson 1995) and acoustic fluidization (Melosh 1979).

Strength models for rocky materials are relatively well-established and have been implemented in hydrocodes to simulate a number of terrestrial impact craters such as Sudbury, Ries and Chicxulub (Ivanov and Deutsch 1999; Collins et al. 2002; Wünnemann et al. 2005). However, the strength model for ice is still undergoing development, limiting the numerical investigation of impact crater formation on the icy satellites. The lack of a definitive strength model for rock during impact implies that numerical modeling of complex crater formation is inherently non-unique; the same crater morphology can be produced with quite different strength models. Consequently, in constructing a usable strength model for impacts in ice, we investigate two methods of simulating material weakening during impact: one a purely empirical model in which the strength parameters are altered to approximate the amount of target weakening during crater collapse, and a part-empirical, part-theory based model in which we implement the weakening mechanism of acoustic fluidization (Melosh 1979). We simulate impact crater formation in unlayered H₂O ice using these two models, and test our model results via comparison to actual crater profiles and scaling trends for craters on Ganymede to determine the range of target strength parameters that can produce a reasonable match between the modeled and observed data.

As measurements of craters on Ganymede and the Moon suggest important phenomenological differences between

cratering in rock and ice, we also model impact into rock using the two strength models, and compare the parameters required to recreate the correct morphology of a lunar and Ganymede crater in each case. To directly compare the difference in model strength parameters necessary to recreate impact cratering in ice and rock, the same style of crater must be compared; for bodies of similar gravity, like the Moon and Ganymede, this means the same size crater. However, the contrasting morphological trends on the Moon and Ganymede at large diameters mean that only simple and central peak morphologies on the two bodies can be directly compared. The upper bound for a suitable simulation size is offered by a change in d/D ratio on Ganymede at $D \sim 26$ km, after which craters are believed to be affected by the presence of subsurface rheological changes (Schenk 2002). The s-c transition on the Moon sets a lower bound to our modeled crater size as lunar craters below ~ 15 km will be simple craters. We therefore concentrate on the simulation of a crater between 15 and 26 km in diameter.

Initial Conditions

Lunar impacts involve the collision of asteroids and comets with an averaged impact velocity of ~ 15 km s⁻¹ (Wetherill 1971; Rickmann et al. 2001), while impact in the Galilean system commonly involves Jupiter Family Comets with velocities between 21 and 25 km s⁻¹ (Zahnle et al. 1998). The impactor for lunar simulations was approximated to a gabbro projectile with an impact velocity of 15 km s⁻¹. We modeled our Ganymede impactor as pure water ice with an impact velocity of 15 km s⁻¹ and scaled the projectile size accordingly to produce the same sized crater in both rock and ice (Schmidt and Housen 1987); thus allowing direct comparison to lunar simulations. The structure and composition of both projectiles were simplified to spherical and homogeneous. Due to the 2D axis-symmetric nature of the hydrocode, impact angle was set to 90° instead of the more statistically likely 45°. It is acknowledged that variation from this value will have an effect on the subcrater stress regime.

The target structure was simplified to a homogeneous, unlayered half-space to prevent complexities arising from additional layering and multi-material effects. We approximated the thermodynamic response of the lunar crust using the Tillotson EoS for gabbroic anorthosite (Tillotson 1962; Ahrens and O'Keefe 1982). For Ganymede simulations we used the Tillotson EoS for ice Ih (Tillotson 1962; Ivanov et al. 2002), as the thermodynamic properties of other compositional candidates for the Ganymede surface remain undefined. The Tillotson EoS for ice is severely limited in its applicability for hypervelocity impact; it includes no solid-state or liquid phase changes and is overly simplistic in its treatment of vapor. However, as the focus of our study was late stage collapse, rather than early time phenomena where an accurate EoS is paramount, this simple thermodynamic prescription was deemed sufficient.

Standard strength parameters for gabbro were used to form our static strength model for lunar simulations (Collins et al. 2004, 2008). The static strength model for ice employed in iSALE was derived from low temperature (77 K), high-pressure laboratory data (Durham et al. 1983; Beeman et al. 1988; Rist and Murrell 1994; Weiss and Schulson 1995) and takes account of the material strength dependence on pressure, damage and thermal softening. In a slight modification of Collins et al. (2004), the static strength of damaged ice was represented not using a simple Coulomb model, but rather the Lundborg (1968) approximation:

$$Y_d = Y_{d0} + \frac{\mu_d P}{1 + \mu_d P / (Y_m - Y_{d0})} \quad (1)$$

Where Y_{d0} is the effective cohesion of the damaged ice, μ_d is the coefficient of friction at low pressure, and Y_m is the limiting strength at high pressure. Table 2 lists the static rock and ice strength model parameters used in this work (see Collins et al. 2004, 2008, for further parameter descriptions).

Weakening During Impact

We tested two models for weakening the target material. One approach employed the static strength parameters defined in Table 2, and incorporated the mechanism of acoustic fluidization to weaken the target during impact. Acoustic fluidization during impacts was first suggested by Melosh (1979) as an extension of existing models of earthquake induced landslides (Seed and Goodman 1964). The basic concept involves rock debris flowing in a fluid-like manner when subject to strong vibrations. As the vibrations dissipate, slip events become more localized and less frequent leading to a decrease in the size of the fluidized region, and a larger dynamic viscosity until material strength is regained, allowing crater morphology to be ultimately retained.

iSALE adopts a simple mathematical approximation of acoustic fluidization, known as the block model (Ivanov and Kostuchenko 1997), in which the amount and longevity of fluidization can be controlled by two parameters: the kinematic viscosity of the fluidized region, η , and the decay time of the block vibrations, τ (Wünnemann and Ivanov 2003). In the formal derivation of the block model Melosh and Ivanov (1999) relate η to the average block size of the fragmented subcrater rock mass. To determine values for the acoustic fluidization parameters in ice and rock different combinations of η and τ were used, controlling the relative amount of target weakening.

As the nature of target weakening during impact is still a matter of debate, we also used a purely empirical approach to define the effective strength of the damaged target during crater formation. Our empirical model used a simple Mohr-Coulomb criterion in which the cohesion Y_{d0} and friction coefficient μ_d in Equation 2 were varied to produce the correct morphology for a 15 to 20 km crater.

Table 2. Impactor properties and static strength parameters.

Parameter	Moon	Ganymede
Cohesion (yield strength at zero pressure), Y_0	50 MPa	10 MPa
Damaged cohesion, Y_{d0}	10 MPa	0.5 MPa
Von Mises plastic limit (yield strength at infinite pressure), Y_m	2.5 GPa	0.11 GPa
Coefficient of internal friction, μ_i	1.5	2.0
Damaged coefficient of friction, μ_{di}	0.6	0.6
Melt temperature, T_m	1500 °K	273 °K
Thermal softening parameter, ξ	1.2	1.2
Density of impactor and target material, ρ	2940 kg m ⁻³	910 kg m ⁻³
Impactor radius	0.5 km	0.3 km
Impact velocity	15 km s ⁻¹	15 km s ⁻¹
Kinetic energy of projectile	56.3 MJ	33.8 MJ

$$Y_d = Y_{d0} + \mu_d P \quad (2)$$

Comparison to Observations

Hydrocode results must be tested by comparison to observational (ground-truth) data such as scaling trends and depth-diameter (d/D) plots. The best-fit model parameters for simulated impact into ice were determined by comparing the modeled crater morphology to an actual topographic profile of a Ganymede crater (Fig. 6b). To ensure that the simulated ‘best-fit’ crater was representative of the general cratering trend, the simulations were also compared to a representative profile created from the scaling trends in Table 1 (Fig. 6a). Modeled craters were primarily assessed on their fit to d/D trend, rim height and wall slope. Central peak morphology also had to be reproduced, although a strict fit to the central peak dimensions was not critical as the central morphology of impact craters was observed to be particularly variable.

Modeling Results

Both the empirical and the acoustic fluidization models can simulate the correct crater depth, wall slope and approximate central peak dimensions of craters on Ganymede. Measurements of the simulated Ganymede crater are included in Figs. 2 to 5 to show the best-fit model crater dimensions relative to observational data. Figure 6 shows the best-fit simulation results produced for both models using the target weakening parameters presented in Table 3. Figures 6a and 6b show the simulations results relative to a representative crater profile constructed from the scaling trends in Table 2, and an actual crater profile, respectively.

The crater simulated using the acoustic fluidization model has an overly broad rim compared to the representative profile which does not incorporate the breadth of crater rims. This prevents a closer fit of the acoustic fluidization model results (Fig. 6a). The empirical model also displays features

that prevent exact match to all observed crater dimensions, including a subtle pit at the peak center. This pitted morphology was present in all empirical model simulations in which the crater wall slope was correctly reproduced. Craters produced using the empirical model display constant wall slopes and do not reproduce the break in wall slope close to the crater rim, leading to an offset in the modeled and observed crater rim position in Fig. 6b.

A comparison of the best-fit simulation results for central peak craters on Ganymede and the Moon is shown in Fig. 7. Final crater structure (right side) and total plastic strain (TPS; left side) are shown for both the empirical (A) and theory-based (B) best-fit models. The target weakening parameters used to obtain the closest fit to observations of both lunar and Ganymede craters are presented in Table 3.

Empirical Model (A)

The closest fit to lunar scaling trends was achieved using a cohesion of 1 MPa and an effective frictional coefficient of 0.3. An effective friction coefficient of 0.23 in conjunction with a cohesion of 0.05 MPa most accurately recreates the morphology of a ~20 km Ganymede central peak crater (Fig. 7, models A).

The final crater morphology in the Moon-A and Ganymede-A simulations was the result of rapid, large-scale inward collapse of crater wall material that collided to form a central peak. This style of crater formation results in a deep bowl-shaped zone of highly deformed material beneath the crater that extends down to the maximum depth of the crater. This zone of heavily disrupted, inwardly collapsed material is delineated approximately in Fig. 7 by the TPS contour of 1. Note that a large volume of this material experienced a TPS in excess of 2, and that structural uplift beneath the centre of the crater extends to a depth of 3 km; beneath this, any net displacement of material is down.

Acoustic Fluidization Model (B)

A best-fit lunar crater was produced using a decay time of 50 s and a kinematic viscosity of 125,000 m² s⁻¹. The closest fit to Ganymede observational data was achieved using similar parameter values: a decay time of 60 s, and a kinematic viscosity of 100,000 m² s⁻¹.

The final crater morphology in the Moon-B and Ganymede-B simulations was the result of a combination of uplift of the crater floor to form the central peak, and inward collapse of the crater wall to broaden the crater. In this case, the deformation of the subcrater target material is distributed over a larger volume, which results in a substantially smaller zone of high TPS (>2) than in the empirical models (Fig. 7). Also evident is that structural uplift beneath the centre of the crater extends to much greater depths in the B-models than in the A-models. Net displacement of subcrater material is upward to a depth of ~6 km in both ‘B’ models.

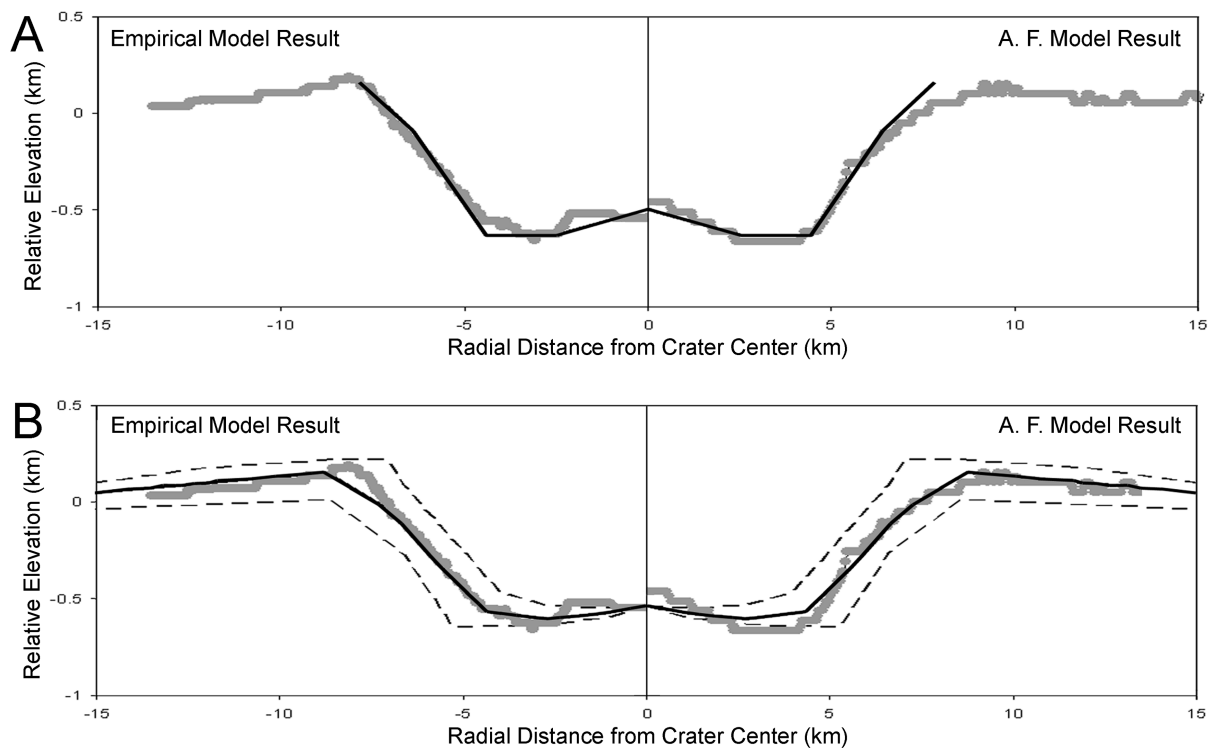


Fig. 6. Final crater profiles produced using the empirical (left) and acoustic fluidization models (right). a) Relative to a representative crater profile constructed from the scaling trends in Table 1 (black line). b) Relative to observational data for a 17 km diameter central peak crater at 38.4 °N, 194.9 °W. The solid black line represents the topographic profile of the crater, averaged from 8 radial profiles. The dotted lines delineate the extent of natural variation in crater topography with azimuth.

Table 3. Best-fit strength model parameters.

Parameter	Moon	Ganymede
Empirical model:		
Cohesion, Y_{d0}	1 MPa	0.05 MPa
Coefficient of friction μ_d	0.3	0.23
Acoustic fluidization model:		
Decay time	50 s	60 s
Kinematic viscosity	125,000 m ² s ⁻¹	100,000 m ² s ⁻¹

Modeling Summary and Implications

We found a best-fit to our scaling trend based profile of a lunar crater using a cohesion of 1 MPa and an effective coefficient of friction of 0.3. For Ganymede we achieved best-fit results using a cohesion of 0.05 MPa and an effective coefficient of friction of 0.23. Both the friction and cohesion values used for ice are less than those used for rock simulations, consistent with the Ganymede surface ice being fundamentally weaker than lunar rock. However, the best fit Y_{d0} values for rock and ice (Table 3) were both 10% of the values expected for damaged rock/ice on the basis of laboratory tests (Table 2). The departure of μ_d from the values in Table 2 was also similar for rock and ice (50 and 40% of the pre-impact damaged coefficient of friction values, respectively). This implies a similar amount of target weakening during impact crater formation in rock and ice.

After investigation of kinematic viscosities spanning the two orders of magnitude between $5 \times 10^3 \text{ m}^2 \text{ s}^{-1}$ and $5 \times 10^5 \text{ m}^2 \text{ s}^{-1}$ we determined a best-fit viscosity of $10 \times 10^4 \text{ m}^2 \text{ s}^{-1}$, with a corresponding decay time of 60 s. These values are similar to the acoustic fluidization parameters used to recreate the lunar crater of $12.5 \times 10^4 \text{ m}^2 \text{ s}^{-1}$ and 50 s. The similar strength parameters used for rock and ice in both strength models suggest that the amount of target weakening occurring during impact does not vary significantly between rock and ice. This could imply that the mechanism of target weakening operates independent of target material. As there are subtle differences in the best-fit parameter values for rock and ice, continued modeling is required to determine whether such a result is robust.

In simulations using the acoustic fluidization model, central peaks are formed primarily by uplift of the target material from depth; in simulations using the empirical model, central peaks are formed by the collision of material collapsing in from the transient crater rim. These two styles of peak formation are differentiated by the size of the highly-deformed zone beneath the crater, the maximum strain beneath the crater, and the depth to the base of the structural uplift (Fig. 7). Central uplifts formed using the acoustic fluidization model extend deeper, and experience lower TPS than central uplifts formed using the empirical model (Fig. 7). Observations of terrestrial and extra-terrestrial

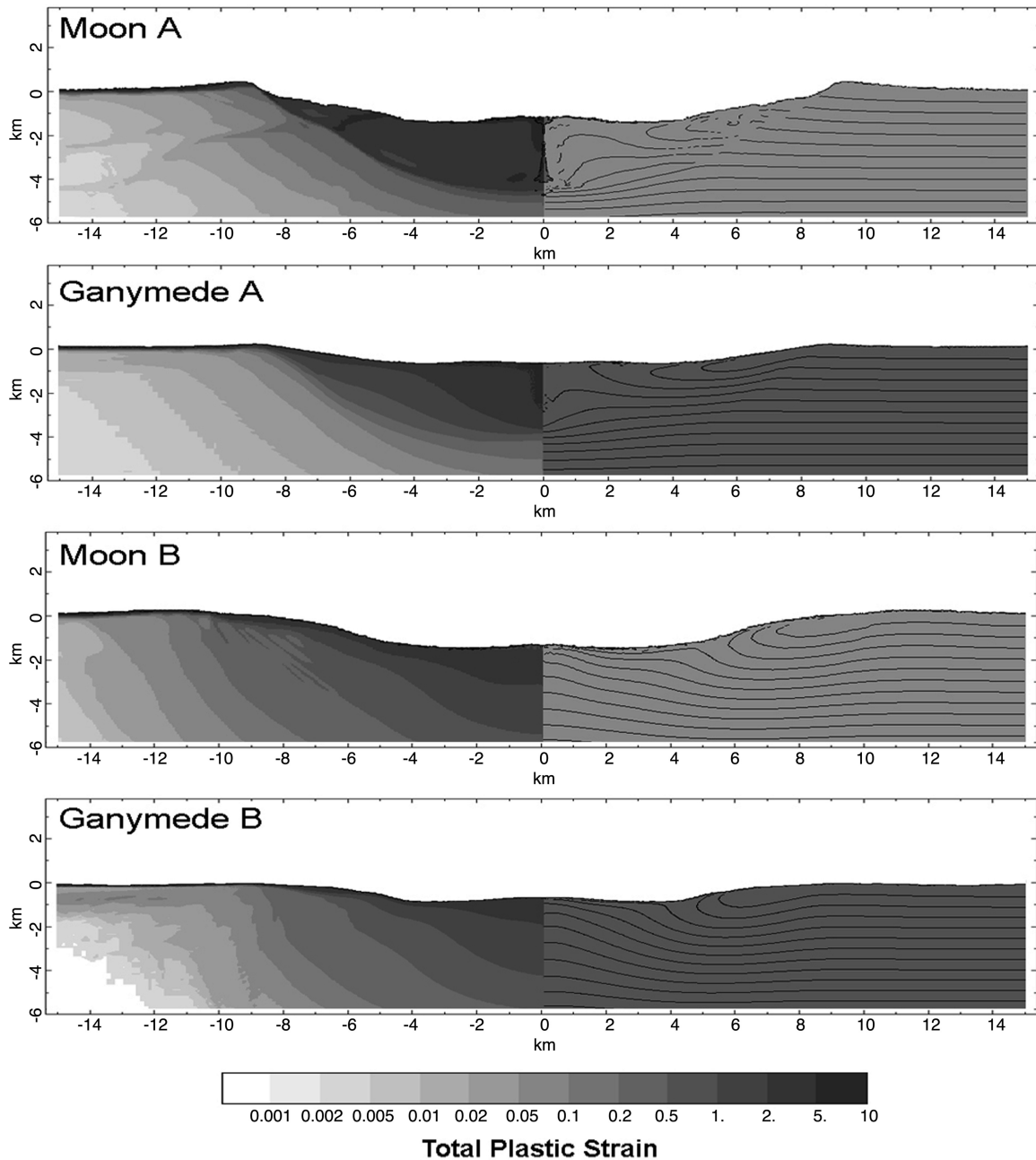


Fig. 7. Best fit simulated crater profiles created using (A) the friction and cohesion values, and (B) the acoustic fluidization parameters in Table 3. Total plastic strain experienced by the target is seen on the left; representative material layers are included on the right hand side to show deformation.

craters may therefore help to select the more appropriate strength model. Observational data from terrestrial impact sites show that material now comprising the central peak has moved inwards, and upwards from depth (e.g., Grieve and Pilkington 1996). As there is no significant upward displacement of crater floor material produced using the empirical model, it suggests that the model incorporating acoustic fluidization to be the more realistic of the two assessed in this work.

The subtle pit produced by the empirical model and the subdued crater rim of the acoustic fluidization model are current flaws which can be explained by assessing the nature of target weakening used in each model. The empirical model utilized a whole-sale weakening of the target which did not decrease in magnitude with time after the impact. As the degree of weakening did not lessen over the course of crater collapse, the material comprising the central peak was too weak for the peak morphology to be maintained, and collapse

continued to form a pit. As no suitable match to crater depth, wall slope and peak dimensions was found without the presence of such a summit pit, it is likely that the empirical model requires a means of lessening the amount of material weakening over time to better reproduce Ganymede crater morphology. This problem is not encountered when using the acoustic fluidization model as the weakening mechanism is transient.

The acoustic fluidization model assumes that the entire weakened portion of the target material acts in a fluid-like manner. This leads to the broader rim morphology seen in Fig. 6, as the rim collapse occurs in a more fluid manner than compared to the dry-friction style of the empirical model. To better reproduce the style of rim collapse, future combination of empirical and acoustic fluidization model styles may be necessary to enable the transient fluid movement of the crater floor, and the dry-friction controlled collapse of the upper crater rim.

CONCLUSIONS

New measurements of Ganymede craters based on Galileo topography have supplemented and updated existing scaling trends for central peak craters on Ganymede. Direct comparison of these with lunar cratering trends has allowed the dependence of crater morphology on target properties to be assessed for rock and ice showing that the crater depth, wall slope and amount of central uplift are all affected by material properties. Minimal difference was noted between craters of the same size in dark and bright terrain. This indicates that the dark terrain of Ganymede does not contain enough rocky material to significantly increase the strength of the surface ice. Scaling trends for fresh craters determined from combined data from the two terrains are thus deemed suitable for comparisons with computer model simulations in pure ice.

The similar rim heights of craters below ~12 km diameter on the Moon and Ganymede imply that a similar amount of rim collapse occurs on both bodies during impacts of this size. This is despite the fact that central peaks are present in craters at these diameters on Ganymede. Together, this suggests that the formation of central peaks at smaller crater diameters on Ganymede than the Moon is not directly linked to rim collapse as suggested by Pike (1980), but dominated instead by enhanced central floor uplift due to weaker material at depth. Conversely, the smaller rim heights of Ganymede craters above ~12 km diameter, relative to the rim heights of craters on the Moon, indicate more significant rim collapse in ice than in rock for larger craters.

Topographic profiles of the largest central peaks reveal a two-tiered morphology, which we suggest is indicative of basal collapse of an over-heightened central peak. If our interpretation is correct, this observation adds support to the hypothesis that peak-ring formation involves the collapse of a large central peak (Melosh 1982; Alexopoulos and McKinnon

1994; Morgan et al. 2000; Collins et al. 2002; Osinski and Spray 2005).

We used our detailed measurements of Ganymede craters to constrain two alternative strength models for use in hydrocode simulations of impacts in ice. In addition, we used existing crater scaling trends for lunar craters to constrain the same two weakening models for use in simulations of impacts in rock. For a crater 15 to 20 km in diameter, a simple strength model (Equation 2) gives reasonable agreement with observation if the effective coefficient of friction is set equal to the tangent of the desired crater wall slope, and a cohesion of 1 and 0.05 MPa is used for the surfaces of the Moon and Ganymede, respectively. Observational results were also recreated for the same size crater using a strength model which incorporated acoustic fluidization. Both strength models suggest that the amount of target weakening occurring during impact varies only subtly between different materials.

The style of crater collapse was substantially different for the two strength models used in our numerical simulations. In the empirical, Mohr-Coulomb model, the central peak formed by inward collapse of the rim; in the acoustic fluidization model, central peaks were formed primarily by uplift of the target material from depth. Hence, if complex crater formation is driven by floor uplift, rather than by rim collapse, as suggested by our observations, the acoustic fluidization model is the more appropriate mechanism for reducing target strength in impact simulations.

Acknowledgments—This work would not have been possible without years of iSALE model development. For this we are especially grateful to Jay Melosh, Boris Ivanov and Kai Wünnemann. Thanks also to Richard Grieve for many helpful discussions, and to Mark Cintala and Thomas Kenkmann for their thorough and constructive reviews of this manuscript.

Editorial Handling—Dr. Gordon Osinski

REFERENCES

- Alexopoulos J. S. and McKinnon W. B. 1994. Large impact craters and basins on Venus, with implications for ring mechanics on the terrestrial planets. In *Large meteorite impacts and planetary evolution*, edited by Dressler B. O., Grieve R. A. F., and Sharpton V. L. GSA Special Paper 293. Boulder: Geological Society of America. pp. 29–50.
- Amsden A. A., Ruppel H. M., and Hirt C. W. 1980. SALE: A simplified ALE computer program for fluid flow at all speeds. Los Alamos National Laboratory LA-8095, Los Alamos, NM, 101 p.
- Beeman M., Durham W. B., and Kirby S. H. 1998. Friction of ice, *Journal of Geophysical Research* 93:7625–7633.
- Breneman H. H. and Belton M. J. S. 1998. Dark terrain on Ganymede: Geological mapping and interpretation of Galileo Regio at high resolution. *Icarus* 135:317–344.
- Bray V. J. 2008. Impact crater formation on the icy satellites. Ph.D. thesis, Imperial College, London, United Kingdom.

- Chyba C. F. 2000. Energy for microbial life on Europa. *Nature* 403: 381–382.
- Collins G. S., Melosh H. J., Morgan J. V., and Warner M. R. 2002. Hydrocode simulations of Chicxulub crater collapse and peak ring formation. *Icarus* 157:24–33.
- Collins G. S., Melosh H. J., and Ivanov B. A. 2004. Damage and deformation in numerical impact simulations. *Meteoritics & Planetary Science* 39:217–231.
- Collins G. S., Kenkmann T., Osinski G. R., and Wünnemann K. 2008. Mid-sized complex crater formation in mixed crystalline sedimentary targets: Insight from modeling and observation. *Meteoritics & Planetary Science* 43. This issue.
- Croft S. K. 1981. Cratering on Ganymede and Callisto: Comparisons with the terrestrial planets. Proceedings, 12th Lunar Planetary Science Conference. pp. 187–189.
- Croft S. K. 1985. The scaling of complex craters. Proceedings, 13th Lunar Planetary Science Conference. *Journal of Geophysical Research* 90:C828–C842.
- Durham W. B., Heard H. C., and Kirby S. H. 1983. Experimental deformation of polycrystalline H₂O ice at high pressure and low temperature: Preliminary results. Proceedings, 14th Lunar Planetary Science Conference. *Journal of Geophysical Research* 88:B377–B392.
- Efford N. 1991. Sources of error in the photoclinometric determination of planetary topography—A reappraisal. *Earth, Moon, and Planets* 54:19–58.
- Grieve R. A. F. 1987. Terrestrial impact structures. *Annual Review of Earth Planetary Sciences* 15:245–270.
- Grieve R. A. F. and Pilkington, M. 1996. The signature of terrestrial impacts. *AGSO Journal of Australian Geology and Geophysics*. 16:399–420.
- Hale W. and Grieve R. A. F. 1982. Volumetric analysis of complex lunar craters: Implications for basin ring formation. Proceedings, 13th Lunar Planetary Science Conference. *Journal of Geophysical Research* 87:A65–A76.
- Hale W. and Head J. W. 1980. Central peaks in Mercurian craters: Comparisons to the Moon. Proceedings, 11th Lunar Planetary Science Conference. pp. 2191–2205.
- Head J. W. 1976. The significance of substrate characteristics in determining the morphology and morphometry of lunar craters. Proceedings, 7th Lunar Science Conference. pp. 2913–2929.
- Ivanov B. A. and Deutsch A. 1999. Sudbury impact event: Cratering mechanics and thermal history. In *Large meteorite impacts and planetary evolution II*, edited by Dressler B. O. and Sharpton V. I. GSA Special Paper 339. Boulder: Geological Society of America. pp. 389–397.
- Ivanov B. A., and Kostuchenko V. N. 1997. Impact crater formation: Dry friction and fluidization influence on the scaling and modification. Proceedings, 27th Lunar Planetary Science Conference. p. 1654.
- Ivanov B. A., Deniem D., and Neukum G. 1997. Implementation of dynamic strength models into 2D hydrocodes: Applications for atmospheric breakup and impact cratering. *International Journal of Impact Engineering* 20:411–430.
- Ivanov B. A., Langenhorst F., Deutsch A., and Hornemann U. 2002. How strong was impact-induced CO₂ degassing in the K/T event? Numerical modeling of shock recovery experiments. In *Catastrophic events and mass extinctions: Impact and beyond*, GSA Special Paper 356. Boulder: Geological Society of America. pp. 587–594.
- Jankowski D. G. and Squyres S. W. 1991. Sources of error in planetary photoclinometry. *Journal of Geophysical Research* 96: 20,907–20,922.
- Lundborg N. 1968. Strength of rock-like materials. *International Journal of Rock Mechanics and Mining Sciences* 5:427–454.
- McEwen A. S. 1991. Photometric functions for photoclinometry and other applications. *Icarus* 92:298–311.
- McKinnon W. B. 1978. An investigation into the role of plastic failure in crater modification. Proceedings, 9th Lunar and Planetary Science Conference. pp. 3965–3973.
- McKinnon W. B., Chapman C. R., and Housen K. R. 1991. Cratering of the Uranian satellites, In *Uranus*, edited by Miner J. T. and Matthews L. D. Tucson: The University of Arizona Press. pp. 629–692.
- Melosh H. J. 1977. Crater modification by gravity: A mechanical analysis of slumping. In *Impact and explosion cratering*, edited by Roddy D. J., Pepin R. O., and Merrill R. B. New York: Pergamon Press. pp. 1245–1260.
- Melosh H. J. 1979. Acoustic fluidization: A new geologic process? *Journal of Geophysical Research* 84:7513–7520.
- Melosh H. J. 1982. A schematic model of crater modification by gravity. *Journal of Geophysical Research* 87:371–380.
- Melosh H. J. 1989. *Impact cratering: A geological process*. New York: Oxford University Press. 265 p.
- Melosh H. J. and Ivanov B. A. 1999. Impact crater collapse. *Annual Review of Earth Planetary Sciences* 27:385–415.
- Melosh H. J., Ryan E. V., and Asphaug E. 1992. Dynamic fragmentation in impacts: Hydrocode simulation of laboratory impacts. *Journal of Geophysical Research* 97:14,735–14,759.
- Moore J. M., Horner V. M., and Greeley R. 1985. The geomorphology of Rhea. Proceedings, 15th Lunar Planetary Science Conference. *Journal of Geophysical Research* 90:C785–C795.
- Moore J. M., Mellon M. T., and Zent A. P. 1996. Mass wasting and ground collapse in terrains of volatile-rich deposits as a solar system process: The pre-Galileo view. *Icarus* 122:63–78.
- Moore J. M., Asphaug E., Belton M. J. S., Bierhaus B., Breneman H. H., Brooks S. M., Chapman C. R., Chuang F. C., Collins G. C., Giese B., Greeley R., Head J. W., III, Kadel S., Klaasen K. P., Klemaszewski J. E., Magee K. P., Moreau J., Morrison D., Neukum G., Pappalardo R. T., Phillips C. B., Schenk P. M., Senske D. A., Sullivan R. J., Turtle E. P., and Williams K. K. 2001. Impact features on Europa: Results of the Galileo Europa Mission (GEM). *Icarus* 151:93–111.
- Morgan J. V., Warner M. R., Collins G. S., Melosh H. J., and Christenson G. L. 2000. Peak-ring formation in large impact craters: Geophysical constraints from Chicxulub. *Earth and Planetary Science Letters* 193:347–354.
- Nycz J. C. and Hildebrand A. R. 2007. Constraining strength properties in Martian surface layers by modeling the peripheral peak ring impact crater morphology (abstract #1360). Bridging the Gap II Conference.
- O'Keefe J. D. and Ahrens T. J. 1982. The interaction of the Cretaceous/Tertiary extinction bolide with the atmosphere, ocean and solid earth. GSA Special Paper 190. Boulder: Geological Society of America. pp. 103–120.
- O'Keefe J. D. and Ahrens T. J. 1993. Planetary cratering mechanics. *Journal of Geophysical Research* 98:17,001–17,028.
- O'Keefe J. D. and Ahrens T. J. 1999. Complex craters: Relationship of stratigraphy and rings to impact conditions. *Journal of Geophysical Research* 104:27,091–27,104.
- Ohnaka M. 1995. A shear failure strength law of rock in the brittle-plastic transition regime. *Geophysical Research Letters* 22:25–28.
- Osinski G. R. and Spray J. G. 2005. Tectonics of complex crater formation as revealed by the Haughton impact structure, Devon Island, Canadian High Arctic. *Meteoritics & Planetary Science* 40:1813–1834.
- Passey Q. R. and Shoemaker E. M. 1982. Craters and basins on Ganymede and Callisto: Morphological indicators of crustal

- evolution. In *Satellites of Jupiter*, edited by Morrison D. Tucson: The University of Arizona Press. pp. 340–378.
- Pearce S. J. and Melosh H. J. 1986. Terrace width variations in complex lunar craters. *Geophysical Research Letters* 13:1419–1422.
- Pierazzo E., Vickery A. M., and Melosh H. J. 1997. A reevaluation of impact melt production. *Icarus* 127:408–423.
- Pike R. J. 1976. Crater dimensions from Apollo data and supplemental sources. *The Moon* 15:463–477.
- Pike R. J. 1977. Size-dependence in the shape of fresh impact craters on the moon. In *Impact and explosion cratering*, edited by Roddy D. J., Pepin R. O., and Merrill R. B. New York: Pergamon Press. pp. 489–509.
- Pike R. J. 1980. Formation of complex impact craters: Mars. *Icarus* 43:1–19.
- Pike R. J. 1985. Some morphologic systematics of complex impact structures. *Meteoritics* 20:49–68.
- Pike R. J. 1988. Geomorphology of impact craters on Mercury. In *Mercury*, edited by Vilas F., Chapman C., and Matthews M. Tucson: The University of Arizona Press. pp. 165–273.
- Rickman H., Fernandez J. A., Tancredi G., and Licandro J. 2001. The cometary contribution to planetary impact rates. In *Collisional proceedings in the solar system*, edited by Marov M. Y. and Rickman H. Dordrecht: Kluwer Academic Publishers. pp. 131–142.
- Rist M. A. and Murrell S. A. F. 1994. Ice triaxial deformation and fracture. *Journal of Glaciology*. 40:305–318.
- Schenk P. M. 1991. Ganymede and Callisto: Complex crater formation and planetary crusts. *Journal of Geophysical Research* 96:15,635–15,664.
- Schenk P. M. 2002. Thickness constraints on the icy shells of the Galilean satellites from a comparison of crater shapes. *Nature* 417:419–421.
- Schenk P. M. and McKinnon W. B. 1991. Dark ray and dark floor craters on Ganymede and the provenances of large impactors in the Jovian system. *Icarus* 89:318–346.
- Schenk P., Wilson R., Hargitai H., McEwen A., and Thomas P. 2001. The mountains of Io: Global and geologic perspectives from Voyager and Galileo. *Journal of Geophysical Research* 106: 33,201–33,222.
- Schenk P. M. 2002. Thickness constraints on the icy shells of the Galilean satellites from a comparison of crater shapes. *Nature* 417:419–421.
- Schenk P. M., Wilson R. R., and Davies A. G. 2004. Shield volcano topography and rheology of lava flows on Io. *Icarus* 169:98–110.
- Schmidt R. M. and Housen K. R. 1987. Some recent advances in the scaling of impact and explosion cratering. *International Journal of Impact Engineering* 5:543–560.
- Seed H. B. and Goodman R. E. 1964. Earthquake stability of cohesionless soils. *Journal of the Soil Mechanics and Foundation Division* 90 (SM6), ASCE, 4128.
- Showman A. P., Mosquera I., and Head J. W. 2004. On the resurfacing of Ganymede by liquid-water volcanism. *Icarus* 172: 625–640.
- Smith D. E., Zuber M. T., Neumann G. A., and Lemione F. G. 1997. Topography of the Moon from the Clementine lidar. *Journal of Geophysical Research* 102:1591–1611.
- Spray J. and Thompson L. 1995. Friction melt distribution in a multi-ring impact basin. *Nature* 373:130–132.
- Tillotson J. M. 1962. Metallic equation of state for hypervelocity impact. General Atomic Report GA-3216. Advanced Research Project Agency, San Diego. 141 p.
- Turtle E. P. and Pierazzo E. 2001. Thickness of a European ice shell from impact crater simulations. *Science* 294:1326–1328.
- Weiss J. and Schulson E. M. 1995. The failure of fresh-water granular ice under multi-axial compressive loading. *Acta Metallurgica et Materialia* 43:2303–2315.
- Wetherill G. W. 1971. Cometary versus asteroidal origin of chondritic meteorites. In *Physical studies of minor planets*, edited by Gehrels T. NASA SP-267. pp. 447–460.
- Wood C. A. 1973. Central peak heights and crater origins. *Icarus* 20: 503.
- Wünnemann K. and Ivanov B. A. 2003. Numerical modelling of impact crater depth-diameter dependence in an acoustically fluidized target. *Planetary and Space Science* 51:831–845.
- Wünnemann K., Morgan J., and Jodicke H. 2005. Is Ries crater typical for its size? An analysis based upon old and new geophysical data and numerical modeling. In *Large meteorite impacts III*, edited by Kenkmann T., Hörz F., and Deutsch A. Boulder: Geological Society of America. pp. 67–84.
- Zahnle K., Dones L., and Levison H. F. 1998. Cratering rates on the Galilean satellites. *Icarus* 136:202–222.